

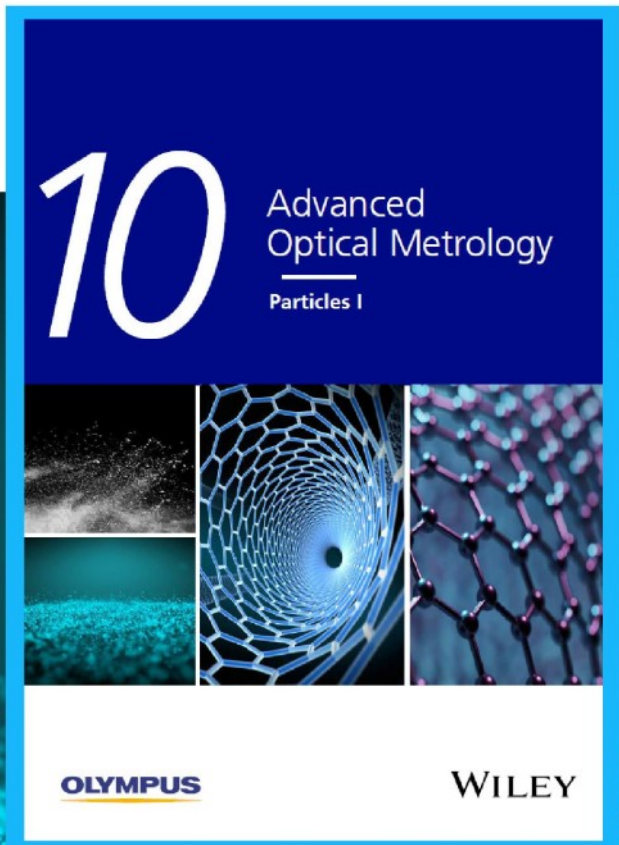


Particles I

Access the latest eBook →

Particles: Unique Properties,
Uncountable Applications

**Read the latest eBook and
better your knowledge with
highlights from the recent
studies on the design and
characterization of micro-
and nanoparticles for
different application areas.**



Access Now

This eBook is sponsored by

OLYMPUS

WILEY

4D Printing of Shape Memory Polymers: From Macro to Micro

Christoph A. Spiegel, Maximilian Hackner, Viktoria P. Bothe, Joachim P. Spatz, and Eva Blasco*

A novel and versatile shape memory ink system allowing 4D printing with light at the macroscale as well as the microscale is presented. Digital light processing (DLP) and direct laser writing (DLW) are selected as suitable 3D printing technologies to cover both regimes. First, a system based on monofunctional isobornyl acrylate and two crosslinkers consisting of a soft and a hard diacrylate is identified and proven to be compatible with both printing techniques. Employing DLP, a large variety of structures exhibiting distinct complexity is printed. These structures range from simple frames to more demanding 3D geometries such as double platform structures, infinity rings, or cubic grids. The shape memory effect is demonstrated for all the 3D geometries. Excellent shape fixity as well as recovery and repeatability is shown. Furthermore, the formulation is adapted for fast 4D printing at the microscale using DLW. Importantly, the 4D printed microstructures display remarkable shape memory properties. The possibility of trapping and releasing microobjects, such as microspheres, is ultimately demonstrated by designing, smart box-like 4D microstructures that can be thermally actuated—evidencing the versatility and potential of the reported system.

application of an external stimulus.^[1–3] Thermoresponsive SMPs can exhibit a thermally induced shape memory effect (SME) based on glass transition temperatures (T_g) or melting points (T_m). This class of materials permits controlled shape change from their permanent shape to an arbitrary temporary shape, which can be recovered into the initial permanent shape by temperature. In contrast to thermoresponsive hydrogels, SMPs can be actuated not only in aqueous environments but also at ambient or vacuum conditions, without the necessity of swelling reagents.^[4] Furthermore, the mechanical properties as well as stability are superior. Thus, due to these excellent features, SMPs have great potential for applications in the fields of aerospace technology,^[5,6] biomedical devices,^[7,8] flexible electronics,^[9] and soft robotics.^[3,10,11]

1. Introduction

Shape memory polymers (SMPs) are a class of stimuli-responsive, smart materials capable of controlled shape change upon

With the rise of 4D printing in the recent decade, SMPs have been established as one of the most promising functional materials to achieve the incorporation of the fourth dimension.^[12] This additional dimension (time) refers to the ability of the 3D printed structures to change their properties over time—shape in the case of SMPs—upon the exposure to external stimuli, e.g., temperature. At the macroscale, several examples using vat photopolymerization 3D printing techniques such as stereolithography (SLA) or digital light processing (DLP), have been demonstrated. For instance, using microstereolithography Ge et al. employed methacrylate-based comonomers for the fabrication of various 3D printed SMP structures including an Eiffel Tower, a microgripper as well as stent structures envisioning potential biomedical applications.^[13] Applying an ink formulation based on methacrylated polycaprolactone (PCL), Zarek et al. printed cardiovascular and tracheal stents in addition to smart SMP electrical circuits.^[14,15] Furthermore, Zhang et al. reported an acrylate-based ink system, utilizing *tert*-butyl acrylate and aliphatic urethane diacrylate allowing 1240% stretching at the programming temperature with excellent shape fixity and good shape recovery.^[16] In addition to SMPs displaying one-way SME, a printable triple SMP system^[17] as well as self-healing^[18–20] and recyclable^[21,22] SMPs have been recently described.

Shifting from macro to microdimensions, direct laser writing (DLW) has been established as the method of choice for 3D printing of precise and complex geometries in the micro- and nanometer scale.^[23–27] DLW, also known as two-photon lithography or 3D laser printing, relies on a multiphoton polymerization process using a femtosecond pulsed laser, enabling printing of structures with submicrometer resolution.

C. A. Spiegel, V. P. Bothe, E. Blasco
Institute of Organic Chemistry
Heidelberg University
69120 Heidelberg, Germany
E-mail: eva.blasco@oci.uni-heidelberg.de

C. A. Spiegel, V. P. Bothe, E. Blasco
Centre for Advanced Materials
Heidelberg University
69120 Heidelberg, Germany

C. A. Spiegel, E. Blasco
Institute of Nanotechnology (INT)
Karlsruhe Institute of Technology (KIT)
76344 Eggenstein-Leopoldshafen, Germany

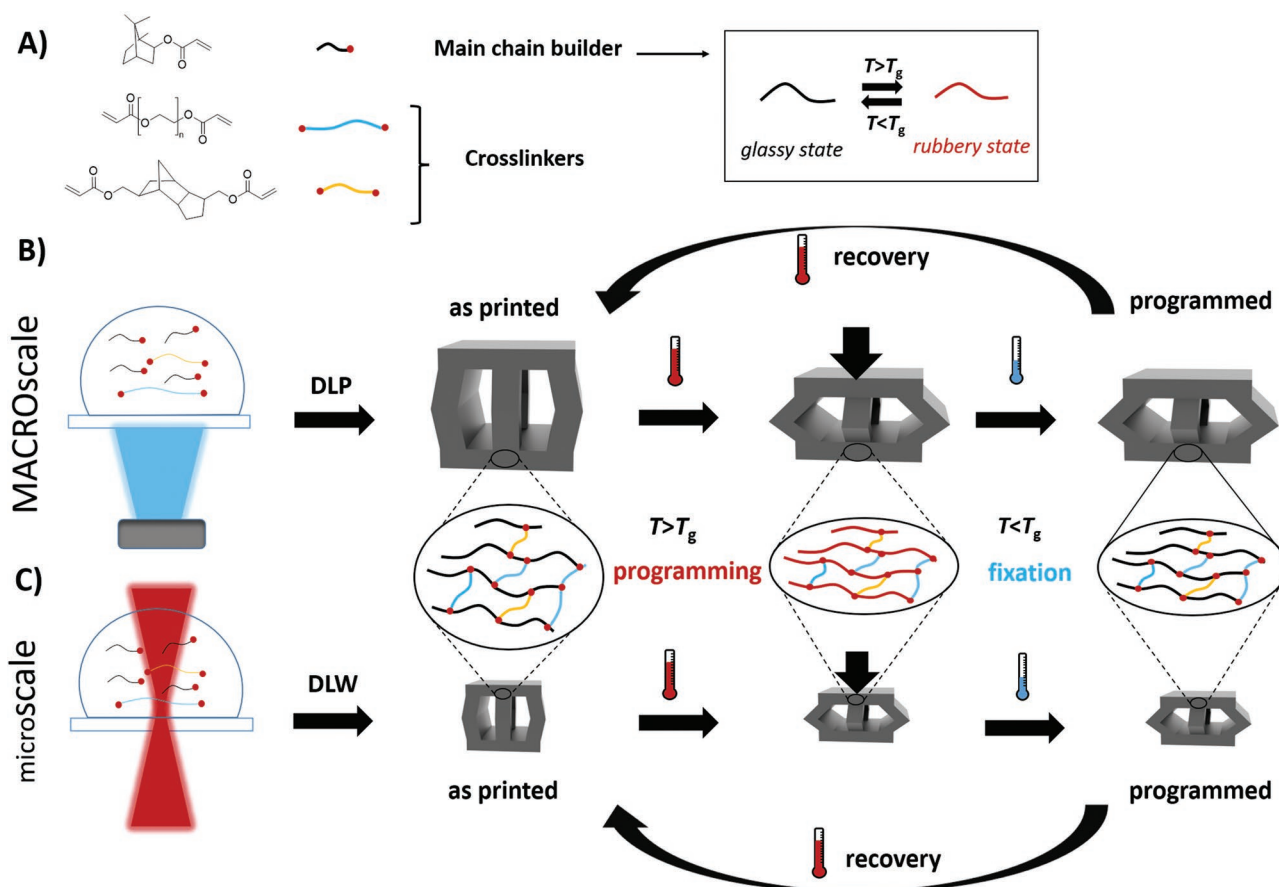
M. Hackner, J. P. Spatz
Department of Cellular Biophysics
Max Planck Institute for Medical Research
69120 Heidelberg, Germany

M. Hackner, J. P. Spatz
Institute of Molecular Systems Engineering (IMSE)
Heidelberg University
69120 Heidelberg, Germany

 The ORCID identification number(s) for the author(s) of this article can be found under <https://doi.org/10.1002/adfm.202110580>.

© 2022 The Authors. Advanced Functional Materials published by Wiley-VCH GmbH. This is an open access article under the terms of the Creative Commons Attribution License, which permits use, distribution and reproduction in any medium, provided the original work is properly cited.

DOI: 10.1002/adfm.202110580



Scheme 1. Novel SMP ink system for 4D macro- and microscale printing. A) Composition of the core system including Isoba as functional monomer and a dual crosslinker system consisting of PEGDA 575 and Tcdda. The resulting system is selected to exhibit a T_g based SME. Schematic representation of the 4D printing process B) at the macroscale using DLP and C) at the microscale using two-photon DLW. Utilizing an adequate temperature ($T > T_g$), the initial shape can be programmed to an arbitrary temporary shape and recovered on demand to its initial shape.

Although 4D printing at the microscale using DLW has already been established for hydrogels,^[28–30] elastomeric liquid crystals,^[31–33] and composite materials,^[34–37] microprinting of SMPs has only been scarcely explored.^[38]

To date, only two examples of DLW fabricated SMPs at the microscale have been reported. Zhang et al. have developed an ink based on commercially available Vero Clear mixed with elastomer, providing a T_g -based SME.^[39] Applying this ink 3D color filters composed of a base layer and a sub-micron grid were fabricated. Due to scattering and interference of incident light with the printed nanostructures, certain wavelengths were preferentially transmitted in dependence of the geometric parameters of the grid structure. By programming and fixing the grid in a compressed shape the color filter effect vanishes leading to transparent structures. Upon recovery of the permanent shape all colors reappear. In a second example, Elliott et al. have developed an acrylate/methacrylate-based ink composed of benzyl methacrylate (BMA) as first chain builder, an amine-functionalized methacrylate as second chain builder and synthetically modified pentaerythritol triacrylate as crosslinker.^[40] The authors demonstrated SME in various printed microstructures such as flowers, cubic lattices, and cylindrical pillars employing the

described material. However, to the best of our knowledge, no study has been conducted on the investigation of the printability of SMPs that are suitable for both macroscale as well as microscale printing.

Herein, we present simple but versatile printable SMP formulations allowing for 4D printing of programmable structures in two size regimes: macro- and microscale (Scheme 1). To achieve this, we have chosen DLP and DLW as suitable 3D printing technologies for the macro- and microscale, respectively. As a first step, a common functional core system consisting of adequate monomers, crosslinkers, and photoinitiator, which exhibits shape memory response and is compatible with both printing techniques is identified. For development of the ink formulation system, we restrict ourselves to entirely commercially available components to provide maximum accessibility and avoid the necessity of additional chemical modification. Once optimized the formulations for both techniques, a range of different structures featuring different levels of complexity are manufactured at the macro- and microscale. The viscoelastic properties of the 4D printed structures are evaluated by dynamic nanomechanical analysis (DnMA). The shape memory effect is demonstrated showing excellent shape fixity as well as shape recovery and repeatability for both size regimes. We

believe this novel system allowing printing at different scales will open new possibilities in the application of SMPs.

2. Results and Discussion

2.1. Identification of Functional System

In order to develop SMP inks enabling 3D macro- and micro-fabrication, the identification of suitable functional components was conducted as first step. Thereby we defined three criteria the SMP ink must fulfill: i) good printability by applying the two selected 3D fabrication methods (DLP and DLW), ii) adequate shape memory response in terms of programmability, shape fixation as well as recovery and iii) easy access to the components of the ink.

Permitting 3D printability by DLP technology as well as DLW technique, the functional monomers of the system must be compatible with both 3D printing methods. Although both technologies are based on photopolymerization of a liquid ink, they differ in curing source, initiation process, type of object construction as well as print speed and dimension of the fabricated objects.^[41,42] DLP utilizes an UV-LED light source allowing initiation of photopolymerization based on linear one-photon absorption. Construction of objects in the range of mm and cm is performed by layer-by-layer based curing. In contrast, DLW employs a tightly focused femtosecond pulsed laser in the near infrared regime, allowing initiation based on two-photon absorption. In this case, inks having higher photoreactive group densities as well as high viscosity^[43] are favorable. In addition to printability, the incorporation of the desired functionality in the system, the SME in this case, is a second key element for the selection of the system. The resulting printed SMP structure must exhibit a thermal transition allowing deformability for programming a temporary shape above transition temperature and good fixation of this temporary shape below this temperature. Third, by using exclusively commercially available components for the ink formulation, a good accessibility to the community is ensured.

Facing these three criteria, we designed our system whose transition is based on a glass transition temperature. In particular, we selected isobornyl acrylate (IsobA) as monofunctional monomer, main component and linear chain builder, due to the good mechanical properties and printing performance of its corresponding polymer.^[44,45] In terms of the crosslinker, the selection was narrowed to diacrylate functionalized compounds. After an initial screening, we selected a dual crosslinker system consisting of soft elastomer poly(ethylene glycol) diacrylate (average $M_n = 575 \text{ g mol}^{-1}$, PEGDA 575), incorporating chain flexibility into the final network and tricyclo[5.2.1.0^{2,6}]decanedimethanol diacrylate (TcddA), a stiffer system. The right balance between both crosslinkers will allow for a fine tuning of the final mechanical properties as well as the transition temperature of the resulting printed SMP structure. This point will be more extensively discussed in the next sections.

The photoinitiator is also a key component in inks for photopolymerization-based printing techniques. Although it is usually present in small concentrations, its efficiency is critical to initiate the photopolymerization process and therefore, to achieve good and fast printability. Phenylbis(2,4,6-trimethylben-

zoyl)phosphine oxide (Irg819) was selected as a promising candidate as it is commonly used in both printing methods, DLP^[46] and DLW.^[47] Irg819 possesses a suitable absorption in the range of 360 to 400 nm^[48] that perfectly fits with the DLP curing wavelength of 385 nm and it is also active at the two-photon laser wavelength of 780 nm.^[49]

Once the core ink components were selected, the optimization of the inks for both printing techniques as well as the characterization of the shape memory properties of the printed structures was carried out. In the following, we will focus first on the macroscale and subsequently on the microscale formulation for 4D printing.

2.2. 4D Printing of SMPs at the Macroscale

2.2.1. Formulation and DLP Printing

Employing the mentioned functional system, the following formulation was optimized for macroscopic printing (see **Figure 1A**). The ink consists of a mixture of monomer, IsobA (1, 80 mol%), as the main chain builder and flexible and stiff crosslinkers, PEGDA 575 (2, 3 mol%) and TcddA (3, 14 mol%), respectively. Additionally, further additives in smaller concentrations such as hexyl acrylate, HexA (4, 3 mol%), Irg819 as photoinitiator (5, 2 wt%) and Sudan I (6, 0.05 wt%) as photo-absorber were also incorporated. It was shown that the incorporation of monofunctional HexA improved printability and deformability of the printed objects in the rubber state (see the next section). Additionally, Sudan I allowed for lowering the minimal achievable layer thickness.

As a next step, a parameter screening was performed using a modified commercial DLP printer equipped with a 385 nm high power UV-LED. Utilizing a home-made aluminum print head offering a $2.5 \times 2.5 \text{ cm}^2$ built area as well as a downscaled resin tray, printing was possible with 2 to 5 g of ink, allowing screening and testing at research and development scale. Exact description of these modifications is provided in the Experimental section. Curing intensities of 8.0 and 13.0 mW cm^{-2} were identified and further explored in terms of resulting cure depths at different irradiation times. The corresponding Jacobs working curves were generated by semilogarithmic depiction of curing energy versus cure depth for each intensity employed (see **Figure 1B** for 13.0 mW cm^{-2} and **Figure S1**, Supporting Information for 8.0 mW cm^{-2}). In both cases, the system exhibited the expected linear relationship and enabled access to the critical exposure (E_c) and the penetration depth (D_p). E_c is a material property of the ink describing the exposure necessary for the ink to reach the gel point. Below E_c the ink remains liquid, above the E_c at least partial polymerization is observed.^[50] For 8.0 mW cm^{-2} and E_c of $4.3 \pm 1.1 \text{ mJ cm}^{-2}$ and a D_p of 0.09 mm were calculated. A slightly higher value of $4.9 \pm 1.2 \text{ mJ cm}^{-2}$ for E_c and a value of 0.08 mm for D_p was determined for 13.0 mW cm^{-2} .

Based on the obtained parameters (E_c and D_p and working curves), we proceeded with the 3D printing experiments employing the described formulation. Good printability was achieved with a minimal z layer thickness of 50 and 100 μm applying each of the two curing conditions (8.0 mW cm^{-2} , 13.0 mW cm^{-2}). Aiming at a z layer thickness of 50 μm , excellent

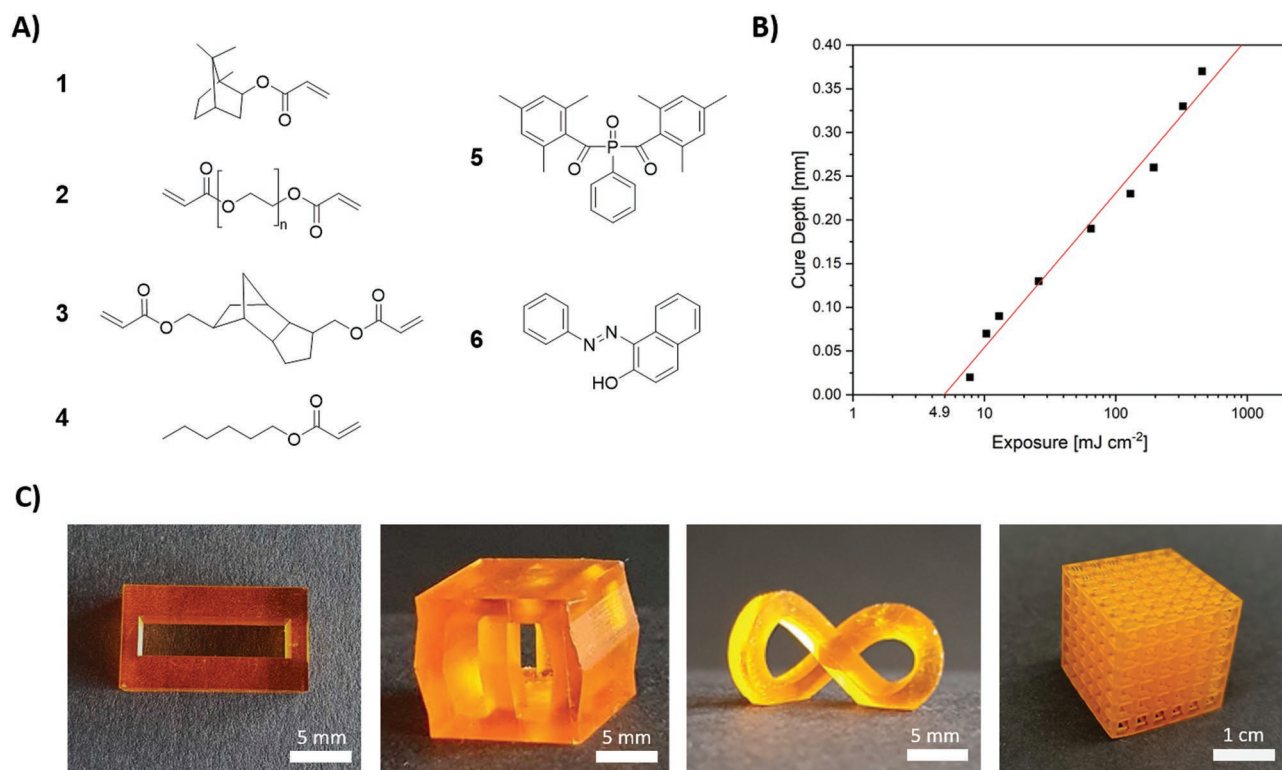


Figure 1. 4D printing at the macroscale via DLP: A) Chemical structures of the components present in the ink formulation: IsobA (1), PEGDA 575 (2), Tcdda (3), HexA (4), Irg819 (5), Sudan I (6). B) Jacob working curve for 13.0 mW cm^{-2} curing condition. Data points correspond to the measured curing thickness at different energy doses. The x-intercept corresponds to the critical exposure. C) Photographs of exemplary 3D printed geometries employing the formulation depicted in (A): frame, double platform structure, infinity ring and cubic grid structure (from left to right).

layer curing times of 1.6 s for 8.0 mW cm^{-2} intensity and 1.5 s for 13.0 mW cm^{-2} were obtained, permitting fast printing at high resolution. To demonstrate the versatility, we designed and successfully printed a large variety of 3D structures of different complexity (see Figure 1C). Efficient 3D fabrication in the centimeter regime was shown not only for simple cylinders and frames, but also for more challenging designs featuring large overhanging parts such as double platform structures, infinity rings or cubic grid structures. All printed structures exhibit low surface roughness, having hardly visible transitions between cured layers. This is a good indication of the effective optimization of the printing parameters as well as excellent performance of the developed ink. This is especially evident in the high quality of the complex 3D cubic grid structure. Having demonstrated the large compatibility towards different designs, the minimal possible feature size to obtain stable structures was evaluated in the next step. A base model containing single quadratic pillars of 74 mm height and different side lengths (0.5, 1, 1.5, 2 mm) was successfully printed for this purpose (see Figure S2, Supporting Information) proving the feasibility of printing minimal feature below 1 mm on the one hand, and the mechanical stability of them, on the other hand.

2.2.2. Shape Memory Effect at the Macroscale

Once the ink formulation as well as the printing parameters were established, the next step was the evaluation of the shape

memory effect (SME). To this end, we evaluated first the transition temperature, the glass transition temperature (T_g) in this case, of the macroscopic 3D printed structures. The transition temperature is a key element in the design of the shape memory tests since it will determine the programming temperature (above T_g) and the fixation temperature (below T_g). We selected a characterization method permitting T_g determination at both size regimes: macro- and microscale. One method suitable for this purpose is dynamic nanomechanical analysis (DnMA) by application of a nanoindentation system.^[51–53] By using this technique, the viscoelastic properties were characterized by following a model described in the literature.^[51] In brief, the indenter-sample system was considered as a mechanical circuit consisting of three elements in parallel: a) black box element corresponding to the sample-indenter load frame, b) a spring element describing the load supporting springs of the nanoindenter, and c) a dashpot element corresponding to the damping between the capacitive plates of the nanoindenter. In addition, the sample was considered as a Voigt solid.^[51,54,55] Thus, it was not necessary to use a specific material model. In particular, DLP 3D printed test samples consisting of cylinders featuring a height of 1 mm and a diameter of 3 mm were utilized. To ensure thermal relaxation of the material, the samples were equilibrated 10 min before measurement. We recorded the displacement amplitude (13–44 nm) and the phase shift (1–26°) in steps of 10 °C within a temperature range from 20 to 150 °C, except for the range between 60 and 80 °C where steps of 5 °C were conducted. The obtained results including

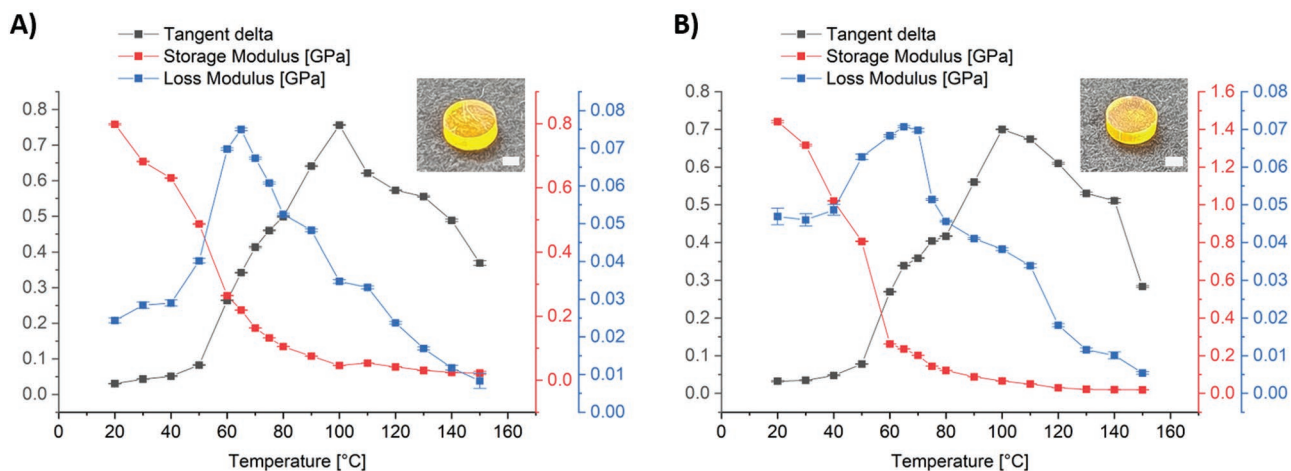


Figure 2. Analysis of viscoelastic properties at the macroscale. Results of the DnMA measurements for a cylindrical sample printed with A) 8.0 mW cm^{-2} , and with B) 13.0 mW cm^{-2} after postcuring (30 s UV light). Data points for tangent delta, storage modulus, and loss modulus are plotted in a temperature range between $20 \text{ }^\circ\text{C}$ and $150 \text{ }^\circ\text{C}$. Error bars represent standard deviation $n = 360$. For each temperature, a different position of the test sample was measured 360 times within one measurement series. An image of the test samples is included as inset within each plot (Scale bar: 1 mm).

the experimental values of storage modulus, loss modulus, and tangent delta are depicted in **Figure 2**. The 3D printed samples fabricated using the two selected irradiation intensities, 8.0 mW cm^{-2} (**Figure 2A**) and 13.0 mW cm^{-2} (**Figure 2B**), were analyzed. In both cases, the storage modulus shows a sharp decrease by increasing the temperature. This behavior is accompanied by a strong growth of the tangent delta starting at $50 \text{ }^\circ\text{C}$, with a maximum at $100 \text{ }^\circ\text{C}$. Furthermore, the loss modulus peak was observed at around $70 \text{ }^\circ\text{C}$, corresponding to the glass transition. Interestingly, T_g of both samples appears in the same range.

Once determined that the printed material exhibits a T_g at around $70 \text{ }^\circ\text{C}$, shape memory tests were performed with the 4D printed structures. The programming and recovery temperature was selected to be $80 \text{ }^\circ\text{C}$ (above T_g) to ensure that the polymer network reaches the rubbery state. For the fixation, the samples were cooled down to rt. At this temperature, the printed structures exhibit a transition to the glass state and the shape can be “frozen.” As a first step, the shape fixity ratio (R_F) and shape recovery ratio (R_R) were evaluated using simple geometries. In particular, rectangular strips ($30 \times 8 \times 0.8 \text{ mm}^3$) were printed as test structures. The test structures were heated in a water bath to $80 \text{ }^\circ\text{C}$ and deformed to an angle of 180° . Afterwards, the bent geometries were fixed by cooling inside a water bath at rt. Pictures of initial, programmed and recovered shapes are included in **Figure S3** (Supporting Information). A R_F of 98% and a R_R of 97% were evaluated proving the excellent shape programming and recovery properties of the printed materials.

As a next step, we tested the SME in more complex 4D printed geometries. These geometries included double platform structures, infinity rings, and frames. By following the procedure indicated above and in the experimental section, the programming and recovery were carried out at $80 \text{ }^\circ\text{C}$ and the fixation at rt. **Figure 3** depicts the photographs taken from the different geometries at their different states: permanent shape, temporary shape, and recovered shape. As a visual demonstration, the whole process (programming + fixation + recovery) was recorded (see **Movie S01**, Supporting Information). An

infinity ring whose dimensions are too large to fit through the neck of a glass bottle was designed and 3D printed. The structure was deformed in $80 \text{ }^\circ\text{C}$ hot water, fixed in water at rt and inserted through the bottleneck. The initial shape of the infinity ring was recovered in preheated water inside the bottle. After recovery, the infinity ring was once again too large to go through the bottle neck being trapped inside, similarly to a decorative ship in a bottle. To prove the repeatability of the SME, the same printed structure was used in seven successive programming/fixation/recovery cycles without apparent loss of its initial properties and/or degradation. We expect the feasibility of an even higher number of cycles. Additionally, to demonstrate the SME under dry conditions, recovery of a 3D printed frame structure by heating with hot air was performed. As before, the frame structure was first programmed into its temporary shape in hot water at $80 \text{ }^\circ\text{C}$ and fixed in water at rt. Reheating via heat gun above T_g allowed complete recovery of the initial shape (see **Movie S02**, Supporting Information).

2.3. 4D Printing of SMPs at the Microscale

2.3.1. Formulation and Microprinting via DLW

Having successfully established a system applicable at the macroscale, the next step was to move toward 4D microprinting. For this purpose, the formulation was slightly adapted to ensure optimal printing results at the microscale. Based on less probable two-photon absorption initiation process, the ink must contain a higher density of photopolymerizable groups per volume for successful microfabrication (see **Figure 4A**). Thus, the mol% of crosslinkers was increased here. In particular, a mixture consisting of IsobA (1, 50 mol%), PEGDA 575 (2, 20 mol%), and TccdA (3, 30 mol%) as well as Irg819 as photoinitiator (4, 2.2 wt%) was employed (see **Figure 4B**). As discussed above, the photoinitiator employed is also suitable for two-photon polymerization. An important difference with respect to the “macroscale formulation” is the absence of additives such as

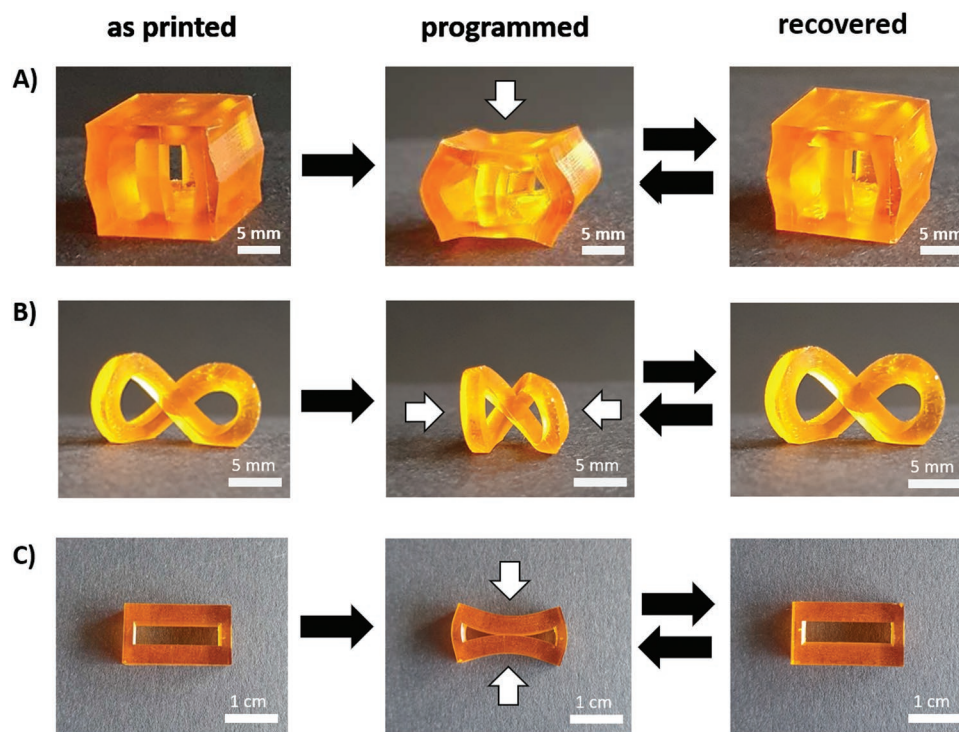


Figure 3. Shape memory tests (programming + fixation + recovery) at the macroscale. Photographs of the 4D printed structures A) double platform, B) infinity ring and C) frame in their initial shape, temporary shape and recovered shape. All structures were programmed and recovered in preheated water at 80 °C and fixed in water at rt.

HexA or Sudan I. The exclusion of HexA is twofold. First, the presence of monofunctional monomers in the mixture reduces the density of photoreactive groups and therefore, the printability using DLW. In addition, HexA reduces the viscosity of the ink. While this is favorable for macroscopic 3D DLP printing, highly viscous inks are preferred in DLW.^[43] Furthermore,

contrarily to one-photon printing, utilization of Sudan I as photoabsorber to improve resolution is not necessary in DLW.

As already pointed out, to increase the photoreactive group density the crosslinker fraction of the ink formulation was increased. A direct consequence is that the crosslinking density of the resulting network will raise, too. Therefore, special

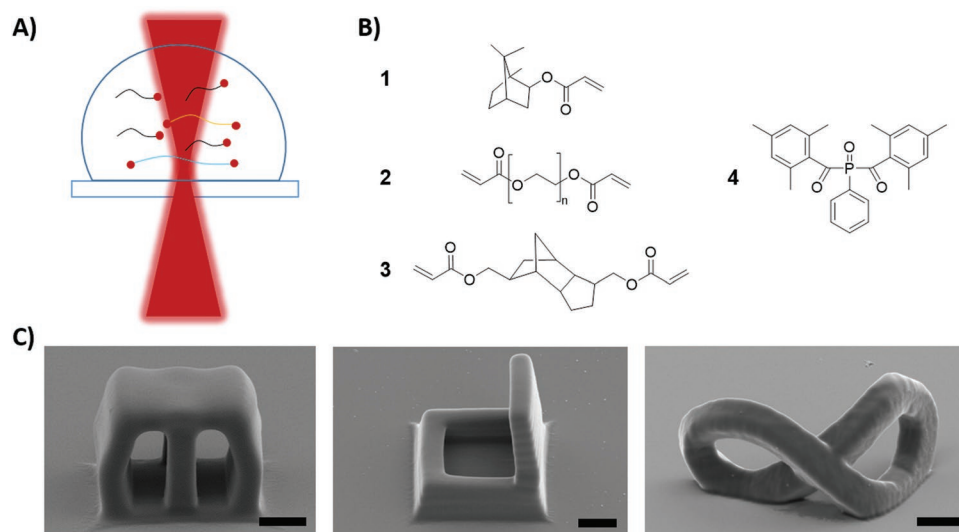


Figure 4. 4D microprinting via DLW: A) Concept of curing by direct laser writing: A femtosecond pulsed laser is tightly focused within a droplet of SMP ink. Curing occurs within the focus allowing high-resolution 3D printing. B) Components of the formulation for 3D structure fabrication at the microscale: IsobA (1), PEGDA 575 (2), Tcda (3), Irg819 (4). C) Scanning electron microscope (SEM) images of fabricated microstructures: double platform structure, trap, infinity ring (left to right). Scale bar: 5 μm .

care has to be taken by selecting the crosslinker concentration. If the crosslinking density is too high the SME response of the cured material would decrease or would not be present at all.^[1] If it is too low, problems regarding mechanical strength of the fabricated structures as well as printability would appear. The previously discussed ink formulation was utilized in a commercial two-photon laser printing device with a central wavelength of 780 nm. After a thorough parameter screening, it was found that average laser power in the range of 19.5 to 22.5 mW and a scan speed of 1000 $\mu\text{m s}^{-1}$ are adequate conditions for printing. Resembling the variety of macrostructures printed using DLP, a wide spectrum of structures of distinct complexity were successfully printed, too. As examples, a microscope double platform structure ($20 \times 20 \times 18 \mu\text{m}^3$ —dimensions of STL model), a box-like structure ($20 \times 20 \mu\text{m}^2$ area, 8 μm height wall, and 15 μm height lid) and the microscopic version of the infinity ring (20 μm length and 15 μm height) were printed using DLW using the optimized conditions (see Figure 4C). All microstructures exhibited high quality and smooth surfaces.

2.3.2. Evaluation of the Transition Temperature

The next step involved the determination of the T_g of the fabricated microstructures. As stated in the prior section, we selected DnMA as a suitable characterization method for micro- and macroscale bridging both worlds in terms of analytics, too. Successful determination of viscoelastic properties of a SMP system has already been demonstrated at the microscale using this characterization method.^[40] Furthermore, this approach has the additional advantage that T_g data is obtained directly from the microstructures, for which measuring methods are otherwise rather limited. Standard methods such as differential scanning calorimetry (DSC) or standard dynamic mechanical analysis (DMA) are unsuitable due to the low amount of effectively polymerized material and the dimensions in the micrometer scale. Utilizing the same model as for the macroscale measurements, the viscoelastic properties of the microstructures were directly determined. In this case, cylindrical pillars featuring a diameter of 10 μm and a height of 20 μm were used as a test structure. Using this bulky design structural effects that possibly distort measured values can be excluded. Data points for displacement amplitude (8–56 nm) and the phase shift (7–25°) were recorded in the range between 20 and 50 °C in steps of 5 °C for the 3D structures fabricated at different laser powers (21.5, 22.0, 22.5 mW). The obtained data for storage modulus, loss modulus, and tangent delta are shown in Figure 5. For all samples, a strong decrease in storage modulus, accompanied by growth of tangent delta was observed by increasing the temperatures. Peaks of loss modulus were observed at around 25 °C corresponding to the glass transition region of the microprinted structures. In comparison to the values of T_g obtained for the macroscopic samples, 70 °C, the microstructures exhibit a lower T_g . The main reason might be due to the higher amount of PEGDA 575 crosslinker in the employed formulation, which is well known to affect mechanical properties of the material, in particular decreasing the T_g .

Additionally, the obtained experimental results correlated with the phenomena observed during an inspection of the

measurements utilizing internal optics of the nanoindentation device. In case of nanoindentation below evaluated T_g a pyramidal imprint was visible after measurement, resulting from a permanent deformation of the material in the glass state. Indentations above evaluated T_g displayed no imprint or deformation of the pillars after stress release by indenter tip removal, confirming the presence of a rubber state allowing immediate recovery.

2.3.3. Shape Memory Effect at the Microscale

In order to prove the shape memory effect at the microscale, the already described three-step procedure consisting of programming–fixation–recovery was performed. Nevertheless, due to the small dimensions, the methodology employed at the macroscale could not be directly applied. The manipulation and observation of the shape changes are more challenging here, since it cannot be followed with the naked eye. Thus, we performed first the programming of the 3D printed microstructures on a glass substrate by compressing at temperatures above the T_g using a polished metal block. The programmed structure was fixed by cooling down to rt. The initial and programmed geometries were crosschecked by SEM inspection (Figure 6A,B). Despite the low transition temperature, room temperature seems to be suitable to perform the fixation of the programmed microstructures. After removal of the block, no recovery of microstructures was observed at rt. Importantly, the shape memory effect observed in the macroscopic samples was successfully translated to the microscale.

To follow the recovery process, an optical microscope with a heating stage was employed. To monitor the process, it is essential that the structural deformation and recovery can be clearly observed via “top-view.” One example of a suitable test geometry is the micrometric version of the double platform structure. It was designed in a way that after compression, the four “microlegs” bend to the outside (see Figure 6A). The compressed microstructures were recovered while being heated above the transition temperature inside the microscope (see Figure 6A and Movie S03, Supporting Information). It should be noted that the temperature indicated in the video is the temperature of the readout of the heating stage. Also, in contrast to the macroscale experiment, where the sample was directly heated to 80 °C ($T > T_g$), heating with a rate of 10 °C min^{-1} was applied. The main reason is to carefully monitor any slight movement of the microstructures during heating.

To further exploit the shape memory properties, we used the printed smart box-like microstructure ($20 \times 20 \mu\text{m}^2$ area, 8 μm height wall, and 15 μm height lid) featuring a lid, which can be closed and opened by adequate programming with temperature. In particular, the structure was printed with the open lid and was programmed to the closed state using the same procedure as described above. Again, good fixation at rt was observed and the recovery was followed by optical microscopy while heating the sample (see Figure 6B and Movie S04, Supporting Information). By comparing both 4D shape memory microstructures, it is evident that the geometry plays a role in the recovery time. While for the first geometry (double platform) the recovery is quite abrupt, for the smart box the lid

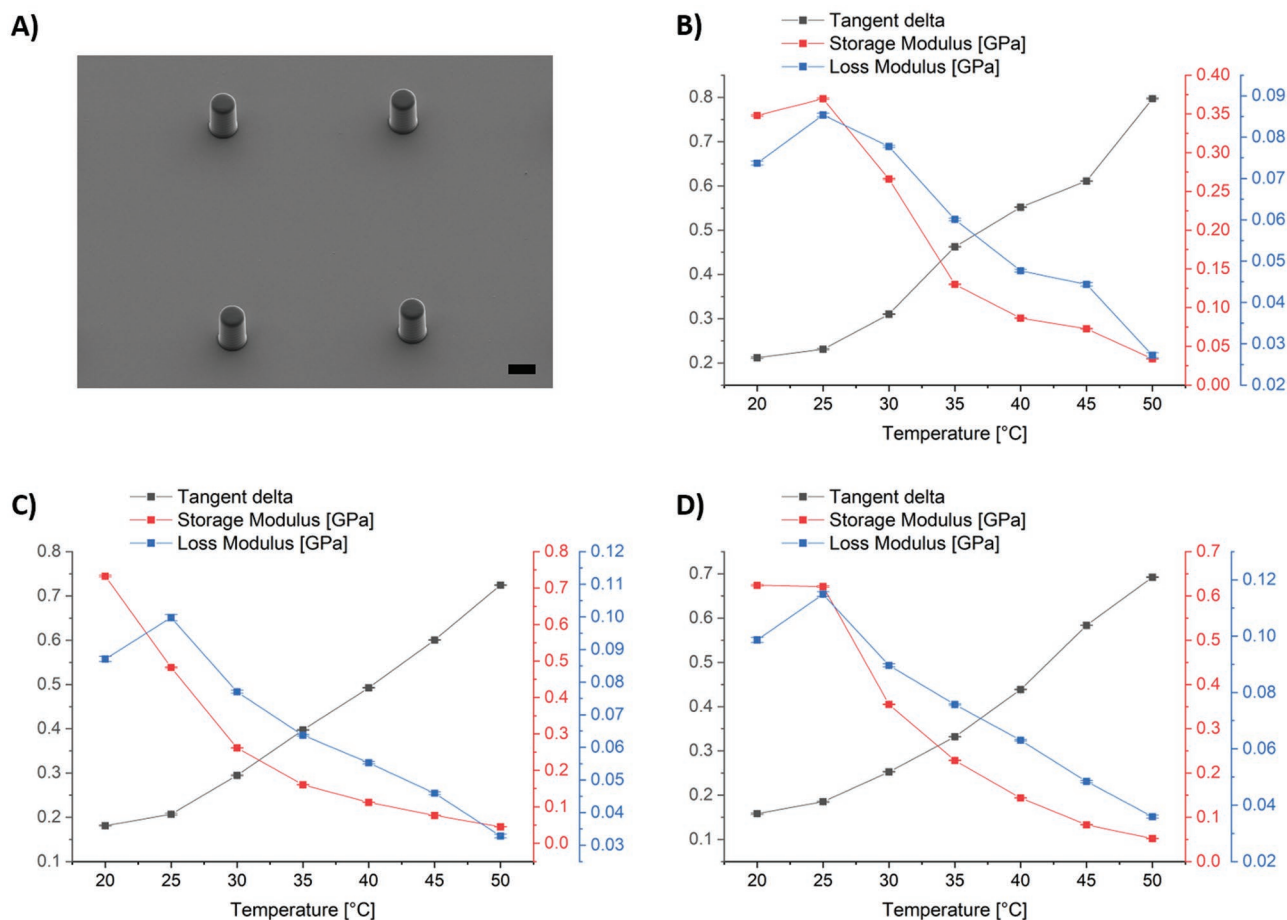


Figure 5. Viscoelastic characterization of the 3D printed microstructures by DnMA. A) SEM image of a cylindrical micropillar (diameter: 10 μm, height: 20 μm) employed as test structure. Scale bar = 10 μm. Measurements were performed on samples fabricated at different laser powers: B) 21.5 mW, C) 22.0 mW, and D) 22.5 mW. For each laser power, the measured values of tangent delta, storage modulus, and loss modulus are depicted within a temperature range from 20 °C to 50 °C. Error bars represent standard deviation $n = 360$.

starts to open at lower temperature and the recovery is slower. This effect, however, was less evident for the different printed geometries at the macroscale.

Furthermore, to demonstrate the functionality of the system, we made use of the thermal actuation of the box-like structure to trap microspheres (see Figure 6C). In particular, poly(styrene-co-divinylbenzene) microspheres (6.0–10.0 μm) were introduced into the micrometric boxes directly after printing by simple deposition of a suspension. After evaporation, the lid of the box was closed employing the mentioned programming method and the microspheres were trapped inside. Afterward, the lid can be opened by temperature on demand to release the microspheres.

3. Summary and Outlook

In summary, we designed a novel and versatile shape memory ink system suitable for 4D printing at the macro- and micro-scale using DLP and DLW printing, respectively. The functional system is based on monofunctional isobornyl acrylate as chain builder and a dual crosslinker system composed of

poly(ethylene glycol) diacrylate ($M_n = 575 \text{ g mol}^{-1}$) as soft segment and tricyclo[5.2.1.0^{2,6}]decanedimethanol diacrylate. It was demonstrated that the formulations were optimized and successfully applied for the 4D printing in both regimes. By using DLP, various 3D structures were printed ranging from simple strips and frames to more demanding geometries such as double platform structures, infinity rings, or cubic grids in the centimeter regime. Fabrication was achieved with layer height of 50 and 100 μm at fast curing speeds, enabling efficient high-resolution macroscale printing. In addition, two-photon DLW was utilized for the printing of the microscopic versions of the previously mentioned 3D geometries such as the double platform structure as well as the infinity ring with high speeds (1000 μm s⁻¹). Viscoelastic properties of printed structures were successfully characterized by DnMA. A glass transition temperature (T_g) of around 70 °C was determined for the macroscopic samples, while a lower T_g of around 25 °C was observed for the microscopic samples. The lower T_g is especially attractive in applications where high temperatures are not desired. Importantly, excellent shape memory effect was demonstrated for all fabricated 3D structures in both size regimes. We believe that the presented approach will open new opportunities in different

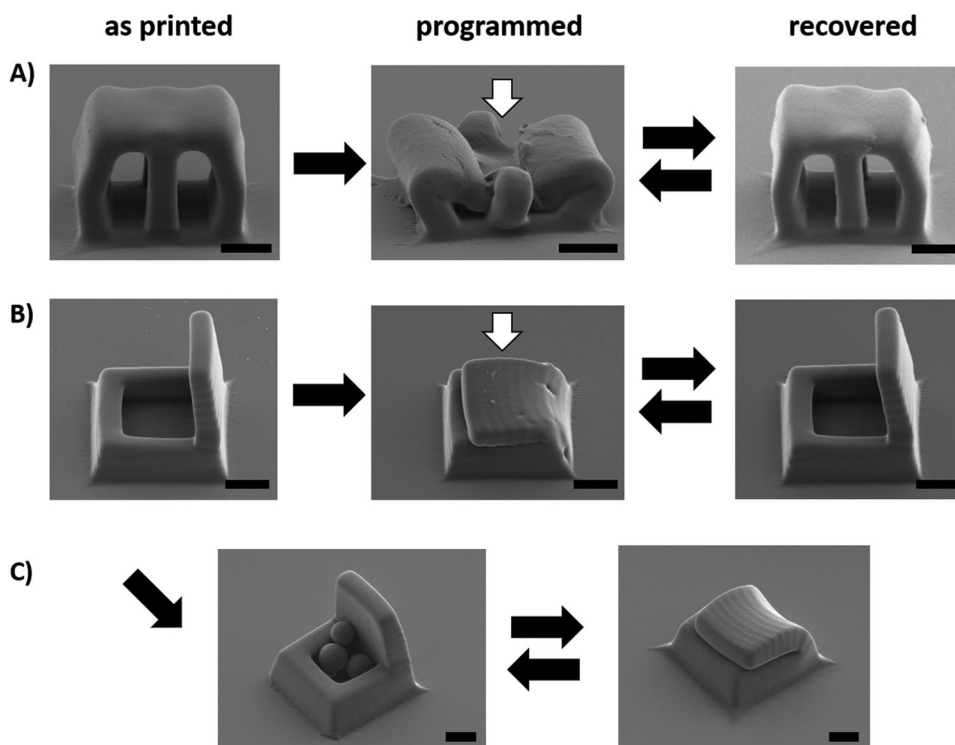


Figure 6. 4D shape memory microstructures. Scanning electron microscope (SEM) images of initial (as printed), programmed (using a metal block ($T > T_g$)) and recovered shapes are displayed for A) double platform structure, B) box-like structure, and C) box-like structures in open, filled state as well as closed state entrapping microspheres. Scale bars: 5 μm .

application fields due to the versatility and accessibility of the materials. Especially, we envision large potential of the system at the microscale in microrobotics and biomedicine due to the remarkable printing performance as well as the possible actuation at low temperatures, which-to the best of our knowledge-is one of the lowest reported in the literature so far.

4. Experimental Section

Materials: Isobornyl acrylate (technical grade, contains 200 ppm monomethyl ether hydroquinone as inhibitor, IsobA), poly(ethylene glycol) diacrylate (average $M_n = 575 \text{ g mol}^{-1}$, PEGDA 575), tricyclo[5.2.1.0^{2,6}] decanedimethanol diacrylate (TcddA), hexyl acrylate (98%, contains 100 ppm hydroquinone as inhibitor, HexA), phenylbis(2,4,6-trimethylbenzoyl)phosphine oxide (97%, Irg819), Sudan I (Dye content $\geq 95\%$), 3-(trimethoxysilyl)propyl methacrylate (98%) and poly(styrene-co-divinylbenzene) microspheres (6.0–10.0 μm avg. part. size) were purchased from Sigma Aldrich. Solvents for development were purchased from Sigma Aldrich or Fisher Scientific. Sylgard 184 (Dow) was purchased from Farnell. All chemicals were used without further purification.

Techniques: *DLP printing:* was performed utilizing a modified commercial Asiga MAX X27 (Asiga Australia) DLP printer, offering a pixel resolution of 27 μm . The commercial build platform (Asiga) was exchanged with a home-made aluminum build platform with a $25 \times 25 \text{ mm}^2$ build area. For tray modification, an aluminum inlet was placed inside a commercial tray. Successively, the space between tray walls and aluminum inlet was filled with Sylgard 184 silicone elastomer and cured at rt for 24 h. For printing, STL files of all fabricated geometries were sliced with desired z layer thickness (50 μm , 100 μm) using the Composer software (Asiga, Australia), and sent to the Asiga MAX X27. Printing was performed at rt under yellow light conditions. After printing the structures were developed for 5 min twice in isopropanol

while sonicating them, successively dried, and finally postcured utilizing a Flash UV chamber (Asiga). Postcuring time was chosen individually depending on the geometry type.

Plasma treatment for surface activation of substrates for microprinting was performed with piezobrush PZ2 handheld plasma cleaner (relyon plasma GmbH A TDK Group Company).

DLW microprinting was performed employing a Photonic Professional GT (Nanoscribe) direct laser writing system. Microfabrication of all structures was performed in oil immersion mode using a 63 \times oil immersion objective (NA = 1.4). Employing Describe software (Nanoscribe) GWL files were generated from STL files of desired geometries and executed by the printer for 3D structure fabrication. Slicing was set to 500 nm and hatching to 250 nm for all microgeometries. Printing was performed with a scan speed of 1000 $\mu\text{m s}^{-1}$ and laser powers in the range of 19.5 to 22.5 mW depending on the structure type. To ensure stability of the samples a custom-built sample holder was used, where the ink was encapsulated. Fabricated structures on substrates were developed for 2 min in acetone and subsequently 1 min in isopropanol, followed by drying in air.

Optical Microscopy: A microscope (Leica DM2700 M, Leica Microsystems) equipped with a 10 \times objective was employed for the inspection of the printed microstructures. Image acquisition and movie recording were performed via analytical microscope software (LAS X, Leica Microsystems) utilizing a FLEXACAM C1 microscope camera (Leica Microsystems).

Heating Stage: A heating stage (LTS 420, Linkam Scientific Instruments) coupled to the optical microscope was employed to induce the recovery of previously programmed microstructures while heating. The temperature program consisted of heating cycle from rt to 110 $^{\circ}\text{C}$ using a gradient of 10 $^{\circ}\text{C min}^{-1}$.

Scanning Electron Microscopy: Scanning electron microscopy (SEM) was performed with Zeiss Supra 55VP (Carl Zeiss AG) at 5 kV. SEM of the micropillars was performed with Zeiss Ultra 55 (Carl Zeiss AG) at 3 kV.

Nanoindentation: Nanoindentation experiments were performed using a Hysitron TI 980 Nanoindenter (Bruker) equipped with a nano-DMA low load head as measurement head. A Berkovich tip geometry was applied utilizing a loading rate of 100 $\mu\text{N s}^{-1}$, a peak force of 500 μN , and a target displacement amplitude of 40 μN at a measurement frequency of 55.75 Hz. Temperature was controlled during experiments by an xSol temperature stage (Bruker). It consists of two ceramic resistor heating modules, one under the sample, one circular around the sample. Both were controlled by a thermocouple and a PID temperature controller. The measurement was thermal drift compensated. Before measurement, the pillars were focused on utilizing the instruments optics and an automatic drift correction was performed. The indentation head was calibrated against air as well as tip area function before measurement. At the macroscale, one position of the test sample was measured 360 times within one measurement series at each temperature. To assure reproducibility and exclude sample and/or thermal inhomogeneity, a different position within the sample was measured as a control. At the microscale, the measurement series was performed in the similar way as described for the macroscale. Thereby, the control measurement series was performed for each temperature at a different microstructure printed using the same conditions.

Procedures: Ink Preparation (Macroscale): Sudan I (3.2 mg, 0.05 wt% in terms of monomer), Irg 819 (128 mg, 2.0 wt% in terms of monomer), TcddA (1227 mg, 4.03 mmol), PEGDA 575 (464 mg, 0.81 mmol), IsobA (4700 mg, 22.56 mmol), and HexA (126 mg, 0.81 mmol) were mixed for 24 h at rt protected by aluminum foil under yellow light conditions. After reaching a homogeneous solution the resin was directly used for DLP printing.

Ink Preparation (Microscale): Irg 819 (7.2 mg, 2.2 wt% in terms of monomer) was added to a mixture containing TcddA (96.4 mg, 317 μmol), PEGDA 575 (121.5 mg, 211 μmol) and IsobA (110.0 mg, 528 μmol) in a brown glass vial under yellow light conditions. The mixture was stirred for 1.5 h at rt to ensure homogeneity and stored protected from the light inside the fridge (at 6 °C) until usage.

Silanization Procedure: The glass slides (Marienfeld, 170 \pm 5 μm strength) were washed with isopropanol and acetone and dried using pressurized N_2 . Subsequently, the surface was activated for one minute by plasma treatment. Afterward, the glass slides were immersed in a 4×10^{-3} M solution of 3-(trimethoxysilyl)propyl methacrylate in toluene for 1.5 h. After washing twice in toluene and in acetone, the methacrylate functionalized glass slides were used as substrate for DLW microfabrication.

Screening for Printing Conditions: Applying the Material Test function of the Asiga MAX X27 (Asiga Australia), data points for generation of the material printing file were evaluated. Thereafter adjustment of the irradiation intensity (8.0 mW cm^{-2} and 13.0 mW cm^{-2}), a droplet of ink was placed on a glass slide (Marienfeld, 170 \pm 5 μm) inside a commercial tray (Asiga) and irradiated. After irradiation for a selected time frame, the polymerized part of the droplet was washed with acetone. Afterward the thickness of the solidified film was measured using a digital caliper. The film thicknesses were noted for several irradiation times and used for the generation of the material printing file and the Jacobs working curves.

Shape Memory Tests (Macroscale): 3D printed macrostructures were heated to 80 °C utilizing a water bath, deformed and fixed in water at rt. Recovery was performed at 80 °C utilizing a preheated water bath. "Dry" recovery was performed by heating the 3D macrostructures above T_g employing a heating gun.

Shape Memory Tests (Microscale): The substrates containing the 3D printed microstructures were fixed via polyimide tape onto a microscope slide and heated inside a drying oven to 109 °C. After ensuring the sample to be above transition temperature, the programming of the sample was executed by positioning a polished metal block (172.9 g) on top of the glass slide to induce deformation by compression and programming of the structure. By cooling to rt while maintaining the stress the temporary shape was fixed. The temporary shape was confirmed by observation via microscope. For recovery the sample was heated up to 110 °C applying a temperature gradient of 10 °C min^{-1} using a heating stage. Recovery was followed by microscopic observation and recorded via analytical microscope software.

Microsphere Trapping: A poly(styrene-co-divinylbenzene) microsphere suspension (1 wt% in isopropanol) was prepared. A drop of the suspension was added to the microtraps in their initial shape. After evaporation of isopropanol and verification of successful loading by observation via microscope, previously described shape memory cycle was performed.

Supporting Information

Supporting Information is available from the Wiley Online Library or from the author.

Acknowledgements

E.B. acknowledges the funding from the Deutsche Forschungsgemeinschaft (DFG, German Research Foundation) via the project BL-1604/2-1 and the Excellence Cluster "3D Matter Made to Order" (EXC-2082/1-390761711 and the Carl Zeiss Foundation through the "Carl-Zeiss-Foundation-Focus@HEiKA. The authors further acknowledge support by the Helmholtz program "Materials Systems Engineering" (MSE) at the Karlsruhe Institute of Technology and the Max Planck Society for general support. The authors thank Prof. Dr. C. Selhuber-Unkel, Dr. M. Taale, and C. Vazquez Martel (Heidelberg University) as well as Dr. M. Hippler (KIT), for the fruitful discussions. The authors also want to thank Dr. J. Thiele's team (Leibniz-Institut für Polymerforschung Dresden) for helpful advice and support regarding modification of the DLP printer and V. Hahn (KIT) for the help with the SEM measurements.

Open access funding enabled and organized by Projekt DEAL.

Conflict of Interest

The authors declare no conflict of interest.

Data Availability Statement

The data that support the findings of this study are available from the corresponding author upon reasonable request.

Keywords

4D printing, digital light processing, direct laser writing, shape memory polymers, two-photon lithography

Received: October 19, 2021

Revised: January 11, 2022

Published online:

- [1] A. Lendlein, S. Kelch, *Angew. Chem., Int. Ed.* **2002**, *41*, 2034.
- [2] A. Lendlein, O. E. C. Gould, *Nat. Rev. Mater.* **2019**, *4*, 116.
- [3] Y. Xia, Y. He, F. Zhang, Y. Liu, J. Leng, *Adv. Mater.* **2021**, *33*, 2000713.
- [4] a) M. Champeau, D. A. Heinze, T. N. Viana, E. R. de Souza, A. C. Chinellato, S. Titotto, *Adv. Funct. Mater.* **2020**, *30*, 1910606; b) Y. Zhang, Y. Li, W. Liu, *Adv. Funct. Mater.* **2015**, *25*, 471.
- [5] Y. Liu, H. Du, L. Liu, J. Leng, *Smart Mater. Struct.* **2014**, *23*, 023001.
- [6] F. Li, Y. Liu, J. Leng, *Smart Mater. Struct.* **2019**, *28*, 103003.
- [7] J. Delaey, P. Dubruel, S. Van Vlierberghe, *Adv. Funct. Mater.* **2020**, *30*, 1909047.
- [8] H. Ramaraju, R. E. Akman, D. L. Safranski, S. J. Hollister, *Adv. Funct. Mater.* **2020**, *30*, 2002014.

- [9] H. Gao, J. Li, F. Zhang, Y. Liu, J. Leng, *Mater. Horiz.* **2019**, *6*, 931.
- [10] A. Lendlein, *Sci. Rob.* **2018**, *3*, eaat9090.
- [11] T. Chen, O. R. Bilal, K. Shea, C. Daraio, *Proc. Natl. Acad. Sci. USA* **2018**, *115*, 5698.
- [12] a) X. Kuang, D. J. Roach, J. Wu, C. M. Hamel, Z. Ding, T. Wang, M. L. Dunn, H. J. Qi, *Adv. Funct. Mater.* **2019**, *29*, 1805290; b) A. Andreu, P.-C. Su, J.-H. Kim, C. S. Ng, S. Kim, I. Kim, J. Lee, J. Noh, A. S. Subramanian, Y.-J. Yoon, *Addit. Manuf.* **2021**, *44*, 102024; c) S. Y. Hann, H. Cui, M. Nowicki, L. G. Zhang, *Addit. Manuf.* **2020**, *36*, 101567.
- [13] Q. Ge, A. H. Sakhaei, H. Lee, C. K. Dunn, N. X. Fang, M. L. Dunn, *Sci. Rep.* **2016**, *6*, 31110.
- [14] M. Zarek, M. Layani, I. Cooperstein, E. Sachyani, D. Cohn, S. Magdassi, *Adv. Mater.* **2016**, *28*, 4449.
- [15] M. Zarek, N. Mansour, S. Shapira, D. Cohn, *Macromol. Rapid Commun.* **2017**, *38*, 1600628.
- [16] B. Zhang, H. Li, J. Cheng, H. Ye, A. H. Sakhaei, C. Yuan, P. Rao, Y.-F. Zhang, Z. Chen, R. Wang, X. He, J. Liu, R. Xiao, S. Qu, Q. Ge, *Adv. Mater.* **2021**, *33*, 2101298.
- [17] B. Peng, Y. Yang, K. Gu, E. J. Amis, K. A. Cavicchi, *ACS Mater. Lett.* **2019**, *1*, 410.
- [18] M. Invernizzi, S. Turri, M. Levi, R. Suriano, *Eur. Polym. J.* **2018**, *101*, 169.
- [19] B. Zhang, W. Zhang, Z. Zhang, Y.-F. Zhang, H. Hingorani, Z. Liu, J. Liu, Q. Ge, *ACS Appl. Mater. Interfaces* **2019**, *11*, 10328.
- [20] E. Rossegger, R. Höller, D. Reisinger, J. Strasser, M. Fleisch, T. Griesser, S. Schlögl, *Polym. Chem.* **2021**, *12*, 639.
- [21] X. Li, R. Yu, Y. He, Y. Zhang, X. Yang, X. Zhao, W. Huang, *Polymer* **2020**, *200*, 122532.
- [22] Z. Chen, M. Yang, M. Ji, X. Kuang, H. J. Qi, T. Wang, *Mater. Des.* **2021**, *197*, 109189.
- [23] S. Maruo, O. Nakamura, S. Kawata, *Opt. Lett.* **1997**, *22*, 132.
- [24] J. K. Hohmann, M. Renner, E. H. Waller, G. von Freymann, *Adv. Opt. Mater.* **2015**, *3*, 1488.
- [25] C. Barner-Kowollik, M. Bastmeyer, E. Blasco, G. Delaittre, P. Müller, B. Richter, M. Wegener, *Angew. Chem., Int. Ed.* **2017**, *56*, 15828.
- [26] M. Carlotti, V. Mattoli, *Small* **2019**, *15*, 1902687.
- [27] a) A. Marino, J. Barsotti, G. de Vito, C. Filippeschi, B. Mazzolai, V. Piazza, M. Labardi, V. Mattoli, G. Ciofani, *ACS Appl. Mater. Interfaces* **2015**, *7*, 46, 25574; b) A. Marino, O. Tricinci, M. Battaglini, C. Filippeschi, V. Mattoli, E. Sinibaldi, G. Ciofani, *Small* **2018**, *14*, 1702959; c) J. K. Hohmann, G. von Freymann, *Adv. Funct. Mater.* **2014**, *24*, 6573; d) P. E. Petrochenko, J. Torgersen, P. Gruber, L. A. Hicks, J. Zheng, G. Kumar, R. J. Narayan, P. L. Goering, R. Liska, J. Stampfl, A. Ovsianikov, *Adv. Healthcare Mater.* **2015**, *4*, 739; e) E. Zerobin, M. Markovic, Z. Tomášiková, X.-H. Qin, D. Ret, P. Steinbauer, J. Kitzmüller, W. Steiger, P. Gruber, A. Ovsianikov, R. Liska, S. Baudis, *J. Polym. Sci.* **2020**, *58*, 1288.
- [28] M. Hippler, E. Blasco, J. Qu, M. Tanaka, C. Barner-Kowollik, M. Wegener, M. Bastmeyer, *Nat. Commun.* **2019**, *10*, 232.
- [29] D. Jin, Q. Chen, T.-Y. Huang, J. Huang, L. Zhang, H. Duan, *Mater. Today* **2020**, *32*, 19.
- [30] C. Lv, X.-C. Sun, H. Xia, Y.-H. Yu, G. Wang, X.-W. Cao, S.-X. Li, Y.-S. Wang, Q.-D. Chen, Y.-D. Yu, H.-B. Sun, *Sens. Actuators, B* **2018**, *259*, 736.
- [31] D. Martella, S. Nocentini, D. Nuzhdin, C. Parmeggiani, D. S. Wiersma, *Adv. Mater.* **2017**, *29*, 1704047.
- [32] H. Zeng, P. Wasylczyk, C. Parmeggiani, D. Martella, M. Burreli, D. S. Wiersma, *Adv. Mater.* **2015**, *27*, 3883.
- [33] M. del Pozo, C. Delaney, C. W. M. Bastiaansen, D. Diamond, A. P. H. J. Schenning, L. Florea, *ACS Nano* **2020**, *14*, 9832.
- [34] H. Ceylan, I. C. Yasa, O. Yasa, A. F. Tabak, J. Giltinan, M. Sitti, *ACS Nano* **2019**, *13*, 3353.
- [35] X. Wang, X.-Z. Chen, C. C. J. Alcântara, S. Sevim, M. Hoop, A. Terzopoulou, C. de Marco, C. Hu, A. J. de Mello, P. Falcaro, S. Furukawa, B. J. Nelson, J. Puigmartí-Luis, S. Pané, *Adv. Mater.* **2019**, *31*, 1901592.
- [36] A. Terzopoulou, X. Wang, X.-Z. Chen, M. Palacios-Corella, C. Pujante, J. Herrero-Martín, X.-H. Qin, J. Sort, A. J. deMello, B. J. Nelson, J. Puigmartí-Luis, S. Pané, *Adv. Healthcare Mater.* **2020**, *9*, 2001031.
- [37] J. Park, C. Jin, S. Lee, J.-Y. Kim, H. Choi, *Adv. Healthcare Mater.* **2019**, *8*, 1900213.
- [38] C. A. Spiegel, M. Hippler, A. Münchinger, M. Bastmeyer, C. Barner-Kowollik, M. Wegener, E. Blasco, *Adv. Funct. Mater.* **2020**, *30*, 1907615.
- [39] W. Zhang, H. Wang, H. Wang, J. Y. E. Chan, H. Liu, B. Zhang, Y. F. Zhang, K. Agarwal, Y. Yang, A. S. Ranganath, H. Y. Low, Q. Ge, J. K. W. Yang, *Nat. Commun.* **2021**, *12*, 112.
- [40] L. V. Elliott, E. E. Salzmänn, J. R. Greer, *Adv. Funct. Mater.* **2021**, *31*, 2008380.
- [41] J. del Barrio, C. Sánchez-Somolinos, *Adv. Opt. Mater.* **2019**, *7*, 1900598.
- [42] S. C. Ligon, R. Liska, J. Stampfl, M. Gurr, R. Mülhaupt, *Chem. Rev.* **2017**, *117*, 10212.
- [43] T. Zandrini, N. Liaros, L. J. Jiang, Y. F. Lu, J. T. Fourkas, R. Osellame, T. Baldacchini, *Opt. Mater. Express* **2019**, *9*, 2601.
- [44] G. D. Zhu, Y. Hou, J. Xu, N. Zhao, *Adv. Funct. Mater.* **2021**, *31*, 2007173.
- [45] W. Voit, T. Ware, R. R. Dasari, P. Smith, L. Danz, D. Simon, S. Barlow, S. R. Marder, K. Gall, *Adv. Funct. Mater.* **2010**, *20*, 162.
- [46] a) Z. Dong, H. Cui, H. Zhang, F. Wang, X. Zhan, F. Mayer, B. Nestler, M. Wegener, P. A. Levkin, *Nat. Commun.* **2021**, *12*, 247; b) S. Lantean, G. Barrera, C. F. Pirri, P. Tiberto, M. Sangermano, I. Roppolo, G. Rizza, *Adv. Mater. Technol.* **2019**, *4*, 1900505; c) I. Roppolo, F. Frascella, M. Gastaldi, M. Castellino, B. Ciubini, C. Barolo, L. Scaltrito, C. Nicosia, M. Zanetti, A. Chiappone, *Polym. Chem.* **2019**, *10*, 5950.
- [47] F. Mayer, D. Ryklin, L. Wacker, R. Curticean, M. Čalkovský, A. Niemeyer, Z. Dong, P. A. Levkin, D. Gerthsen, R. R. Schröder, M. Wegener, *Adv. Mater.* **2020**, *32*, 2002044.
- [48] J. H. Moon, Y. G. Shul, H. S. Han, S. Y. Hong, Y. S. Choi, H. T. Kim, *Int. J. Adhes. Adhes.* **2005**, *25*, 301.
- [49] P. Kiefer, V. Hahn, M. Nardi, L. Yang, E. Blasco, C. Barner-Kowollik, M. Wegener, *Adv. Opt. Mater.* **2020**, *8*, 2000895.
- [50] P. F. Jacobs, *Rapid Prototyping & Manufacturing: Fundamentals of Stereolithography*, Society of Manufacturing Engineers, Dearborn, MI **1992**.
- [51] E. G. Herbert, W. C. Oliver, G. M. Pharr, *J. Phys. D: Appl. Phys.* **2008**, *41*, 074021.
- [52] G. M. Odegard, T. S. Gates, H. M. Herring, *Exp. Mech.* **2005**, *45*, 130.
- [53] G. Huang, H. Lu, *Exp. Mech.* **2007**, *47*, 87.
- [54] W. C. Oliver, G. M. Pharr, *J. Mater. Res.* **2004**, *19*, 3.
- [55] W. C. Oliver, G. M. Pharr, *J. Mater. Res.* **1992**, *7*, 1564.